

The Pre-He White Dwarfs in Eclipsing Binaries. V. TIC 399725538

JAE WOO LEE,¹ KYEONGSOO HONG,¹ MIN-JI JEONG,¹ PAKAKAEW RITTIPRUK,² AND JANG-HO PARK¹

¹*Korea Astronomy and Space Science Institute, Daejeon 34055, Republic of Korea*

²*National Astronomical Research Institute of Thailand, Chiang Mai 50200, Thailand*

ABSTRACT

We present echelle spectra of TIC 399725538 obtained in Korea and Thailand to investigate the physical properties and evolutionary scenarios of EL CVn-type binaries. The time-series spectra yielded the radial velocities (RVs) of the primary component and its atmospheric parameters, $T_{\text{eff},A} = 7194 \pm 70$ K and $v_A \sin i = 68 \pm 9$ km s $^{-1}$. Joint modeling of our RVs and the archival TESS data provided component masses of $M_A = 1.930 \pm 0.054 M_\odot$ and $M_B = 0.211 \pm 0.005 M_\odot$, radii of $R_A = 1.922 \pm 0.020 R_\odot$ and $R_B = 0.207 \pm 0.005 R_\odot$, and luminosities of $L_A = 8.87 \pm 0.39 L_\odot$ and $L_B = 0.546 \pm 0.034 L_\odot$. The surface gravity and distance derived from this modeling are consistent with the model-independent $\log g_B$ obtained from the direct observables and with the Gaia distance. The third light of $l_3 = 0.136 \pm 0.003$ comes mainly from two neighboring stars, TIC 399725539 and TIC 399725544. Comparison with stellar models indicates that TIC 399725538 A lies within the instability region of δ Sct- γ Dor hybrids, whereas its extremely low-mass companion is markedly underluminous compared to theoretical white dwarf (WD) counterparts. Multifrequency analysis of the binary-subtracted residual lights revealed three significant signals, two of which correspond to aliases at two and four times the dominant frequency $f_1 = 0.0848$ day $^{-1}$. The f_1 frequency is likely a γ Dor-type pulsation arising from the brighter A component, though further confirmation is required. Our results demonstrate that TIC 399725538 is a short-period EL CVn system belonging to the thick-disk population, consisting of a main-sequence γ Dor pulsator and a helium-core WD precursor formed through stable mass transfer.

1. INTRODUCTION

The presumed scenario for extremely low-mass white dwarfs (ELM WDs, $M < 0.3 M_\odot$) is that they are formed through non-conservative mass transfer – where a significant fraction of the transferred mass is lost from the system rather than being accreted by the companion – in binary stars, rather than from isolated single stars (T. R. Marsh et al. 1995; M. Kilic et al. 2007; X. Chen et al. 2017). Most of their counterparts are intermediate-mass main-sequence stars, WDs, millisecond pulsars. EL CVn-type eclipsing binaries (EBs) are post-mass transfer systems containing an A/F primary dwarf

(P. F. L. Maxted et al. 2014), some of which exhibit pulsating signals in each component and are accompanied by circumbinary objects (e.g. P. F. L. Maxted et al. 2013; F. Lagos et al. 2020; J. W. Lee et al. 2024). Their study helps us understand the mass transfer and WD formation processes in binary systems. Although new EBs with ELM WD candidates are steadily being discovered by ground- and space-based missions (P. F. L. Maxted et al. 2014; J. van Roestel et al. 2018; Y. Peng et al. 2024; J. Xiong et al. 2025), their physical properties remain largely unknown due to a lack of good spectroscopic data. This paper continues our study for short-period EL CVn-type binaries, initiated with WASP 0131+28 (J. W. Lee et al. 2020). The comprehensive reviews and main goals of this subject are detailed in J. W. Lee et al. (2020, 2024). Here, we focus on TIC 399725538 (HD 287228, 2MASS J04530466+1015099, Gaia DR3 3294443634920790528; $T_p = +10.810$; $V = +11.258$, $(B - V) = +0.402$).

The TESS target was added to our list of spectroscopic observations of EL CVn-type EBs with potential pulsations in 2023. It was first studied in detail by Y. Peng et al. (2024). They searched for EL CVn systems in Gaia EBs (N. Mowlavi et al. 2023), using archive data from TESS (G. R. Ricker et al. 2015) and Gaia (Gaia Collaboration et al. 2023). This survey led to the discovery of four new candidates with typical light curves of the EL CVn type, one of which is TIC 399725538, the program target of this study. Y. Peng et al. (2024) modeled the TESS data observed at 1800-s and 600-s cadences, respectively, in Sectors 5 and 32, and combined the light curve parameters with Gaia spectroscopic elements to obtain the absolute dimensions of TIC 399725538. These results suggested that the EB system is a detached binary with a short period $P_{\text{orb}} = 1.29327$ days and an extreme mass ratio $q = 0.077$, with the secondary component having the characteristics of a pre-ELM WD. Meanwhile, Y. Peng et al. (2024) applied Fourier analysis to the residual light curves obtained through their modeling, but no meaningful pulsation signal was found. This non-detection may be partly attributable to the limitations of the TESS data used in their analysis (e.g., undersampling).

In this article, we report the fundamental properties and possible pulsation signatures of TIC 399725538 based on in-depth analyses of our time-series echelle spectra and the recent TESS photometric data obtained from a higher-cadence mode. The brighter, massive component obscured in the secondary eclipse is denoted by the subscript A, and its hotter counterpart by the subscript B.

2. TESS PHOTOMETRY AND ORBITAL EPHEMERIS

The space-based light curves for TIC 399725538 are available in three observation sectors 5, 32, and 71 of the TESS mission (G. R. Ricker et al. 2015). Sector 5 (S5) was observed at 1800-s cadence between 2018 November 15 and December 11, Sector 32 (S32) at 600-s between 2020 November 20 and December 16, and Sector 71 (S71) at 200-s between 2023 October 16 and November 11. The time-series TESS data were collected from the MAST portal¹. The S5 observations were excluded because their low sampling could introduce light-curve distortions such as amplitude suppression and frequency aliasing. We concentrated our analysis on the SAP data reduced from the SPOC pipeline (J. M. Jenkins et al. 2016). The TESS observations had a significant interruption near the midpoint of each sector, allowing for data downlink. The raw flux data were detrended by introducing a linear least-squares fit to each segment split by this interruption (J. W. Lee et al. 2019, 2024). The corrected fluxes were transformed to magnitudes and are displayed in the top panel of Figure 1.

¹ <https://mast.stsci.edu/portal/Mashup/Clients/Mast/Portal.html>. The observations are available at <http://dx.doi.org/10.17909/c2qe-2177>.

The CROWDSAP values for S32 and S71 are 0.87049663 and 0.85590553, respectively. These mean that 86.3 ± 0.7 % of the observed fluxes in the target aperture originated from TIC 399725538, and the remainder could be contaminated by nearby sources. Two objects, TIC 399725539 ($T_p = +14.01$) and TIC 399725544 ($T_p = +13.14$), are located at distances of 16.33 and 23.08 arcsec from our target, respectively. Given the TESS CCD resolution of 21 arcsec pixel $^{-1}$, it is likely that the neighboring stars affected the TESS measurements. Their combined magnitude of 12.74 mag accounts for about 14 % of the total brightness of the three stars, which matches well with the 13.7 % contamination from the CROWDSAP.

To update the orbital ephemeris reported in [Y. Peng et al. \(2024\)](#), we measured 67 minimum epochs from the TESS data ([K. K. Kwee & H. Van Woerden 1956](#)) as shown in Table 1 which resulted in the following ephemeris via least-squares fitting:

$$\text{Min I} = \text{BJD } 2,460,235.49338(\pm 0.00048) + 1.29327809(\pm 0.00000090)E. \quad (1)$$

The $O - C$ timing residuals calculated using this ephemeris are presented in the fourth column of this table. The phase-folded light curves for S32 and S71 are plotted as blue and green circles, respectively, in the second panel of Figure 1. The two eclipse types, Min I and Min II, are separated by a phase difference of 0.5, indicating that the binary star is probably in a circular orbit.

3. ECHELLE SPECTROSCOPY AND SPECTRAL ANALYSIS

We obtained a total of 33 echelle spectra of TIC 399725538 using two different facilities: the Bohyunsan Optical Astronomy Observatory (BOAO) in Korea and the Thai National Observatory (TNO) in Thailand. The BOAO observations were conducted over five nights, between 2023 November 10 and 2024 March 10, using the echelle spectrograph BOES ([K.-M. Kim et al. 2007](#)) at the Doyak 1.8-m telescope. Twenty-seven target spectra were acquired, each with an integral time of 1800 s, covering a wavelength range of 3600–10,200 Å with a resolving power of $R \approx 30,000$. The remaining six spectra were taken on 2025 January 7 using the TNT 2.4-m telescope and the MRSE spectrograph ([C. Buisset et al. 2018](#); [R. Errmann et al. 2020](#)) at TNO, with the same exposure time of 1800 s. This spectrometer provides a spectral coverage of 3800–9000 Å, with $R \approx 18,000$. The observed raw spectra were pre-processed using the `echelle` routines within `IRAF` in the same way as applied to WASP 0843–11 ([K. Hong et al. 2021](#)) and V389 Cas ([P. Rittipruk et al. 2025](#)). The resulting spectra from both observatories exhibit a typical signal-to-noise ratio (SNR) of ~ 15 , each around 4500 Å.

We adopted the broadening function (BF) method ([S. M. Rucinski 1992, 2002](#)) implemented in the `RaveSpan` software ([B. Pilecki et al. 2012](#)) to yield the radial velocities (RVs) of TIC 399725538. The BF technique is particularly effective for resolving blended spectral lines in close binary systems. The synthetic template spectra were taken from the LTE library of [P. Coelho et al. \(2005\)](#). We focused the BF measurements on the spectral region of 4840–5085 Å, where hydrogen and metallic lines, particularly the H $_{\beta}$ and Mg I triplet, are prominent. This wavelength range was chosen to minimize contamination by strong telluric features. Figure 2 presents BF profiles taken at quadrature phases $\phi = 0.255$ (BJD 2,460,259.1027) and $\phi = 0.748$ (BJD 2,460,317.9378). As seen in the samples, only a single dominant peak associated with the primary star is detected. The absence of companion signatures at the predicted RV positions, indicated by arrows in this figure, is likely due to the limited SNR of the observed spectra and the very low light contribution of the secondary component ($\sim 2.3\%$),

which will be quantified through binary modeling in the next section. The RV measurements for TIC 399725538 A are summarized in Table 2 and plotted in Figure 3.

To reconstruct the representative spectrum of the primary component, we employed the **shift-and-add disentangling** method² (T. Shenar et al. 2020, 2022), optimized for the 3900–5085 Å region of the observed target spectra. This spectral window includes the Balmer and metallic lines such as Ca II K and H (λ 3933.68 and λ 3968.49), H $_{\delta}$, H $_{\gamma}$ and H $_{\beta}$. The reconstructed spectrum was continuum-normalized using the neural-network-assisted SUPPNET algorithm³ (T. Różański et al. 2022). The atmospheric modeling was then performed with the GSSP framework⁴ (A. Tkachenko 2015). In this approach, synthetic spectra were generated using SynthV (V. Tsymbal 1996), based on stellar atmospheres from the LLmodels code (D. Shulyak et al. 2004), and fitted to the reconstructed spectrum using a grid-search optimization method.

The GSSP enables the simultaneous optimization of multiple atmospheric parameters: effective temperature ($T_{\text{eff},A}$), surface gravity ($\log g_A$), metallicity ([M/H]), projected rotational rate ($v_A \sin i$), and turbulence velocities ($v_{\text{mic},A}$, $v_{\text{mac},A}$). The initial temperature and surface gravity of TIC 399725538 A was set at $T_{\text{eff},A} = 7398 \pm 83$ K and $\log g_A = 4.0$, as reported in Y. Peng et al. (2024). Owing to the low SNR of our spectra, the solar metallicity was assumed. The microturbulence and macroturbulence velocities were estimated with the iSpec⁵ (S. Blanco-Cuaresma et al. 2014) to be $v_{\text{mic},A} = 1.91$ km s $^{-1}$ and $v_{\text{mac},A} = 17.3$ km s $^{-1}$, respectively. As the optimal result from the GSSP run, we found the atmospheric parameters of $T_{\text{eff},A} = 7194 \pm 70$ K and $v_A \sin i = 68 \pm 9$ km s $^{-1}$ by fitting a polynomial to the minimum χ^2 values (cf. H. Lehmann et al. 2011). Figure 4 shows the final synthetic model superimposed on the reconstructed spectrum.

4. BINARY MODELING AND ABSOLUTE PARAMETERS

The TESS light curve of TIC 399725538 shows the typical morphology of EL CVn-type EBs, with a box-shaped primary eclipse, a curved-bottom secondary eclipse, and an elliptical variation outside eclipse. To derive a consistent light and velocity solution for the program target, we simultaneously analyzed our ground-based RVs along with the space-based TESS data of S32 and S71 using the Wilson–Devinney (W-D) program, which is widely used to model EB observables (R. E. Wilson & E. J. Devinney 1971; J. Kallrath 2022). During this process, we did not use individual observations between BJD 2458252.7 and 2458253.5 exhibiting anomalous light variations, which we believe were due to instrumental issues. The mass ratio, $q = M_B/M_A = K_A/K_B$, is a key parameter that governs binary star modeling and determines fundamental properties such as mass, which is an essential factor in both star formation and stellar evolution. However, since there were no RV measurements for TIC 399725538 B, we could not directly determine its velocity semi-amplitude K_B and the corresponding q value from the present data. To estimate these parameters, we performed an extensive q -search procedure (e.g. J. W. Lee et al. 2008, 2022a).

To minimize degeneracy in this synthesis, we fixed several modeling parameters to reliable values obtained from our spectroscopic analysis and different independent sources. The surface temperature of TIC 399725538 A was initially set at a central value of $T_{A,\text{eff}} = 7194$ K – derived from our analysis of the disentangled spectrum – to derive the best-fit solution. To account for the uncertainties

² https://github.com/TomerShenar/Disentangling_Shift_And_Add/

³ <https://github.com/RozanskiT/suppnet/>

⁴ <https://fys.kuleuven.be/ster/meetings/binary-2015/gssp-software-package>

⁵ <https://www.blancocuaresma.com/s/iSpec/>

propagated from this parameter, we performed additional analyses by setting $T_{A,\text{eff}}$ to its lower (7124 K) and upper (7264 K) bounds (i.e., ± 70 K). A similar procedure was applied to the rotation-to-orbit velocity ratio of the more massive primary (F_A), which was based on the observed $v_A \sin i$ and the synchronous rotations $v_{\text{sync}} = 2\pi R_A / P_{\text{orb}}$. Specifically, F_A was fixed at 0.92 but varied by its error of ± 0.12 for uncertainty estimation, whereas TIC 399725538 B was assumed to be in synchronous rotation ($F_B = 1.0$).

Because the temperatures of both components likely represent radiative envelopes, we adopted the standard values of $A_{A,B} = 1.0$ (H. Von Zeipel 1924) and $g_{A,B} = 1.0$ (S. M. Rucinski 1969) for the albedo and gravity-darkening parameters, respectively. Logarithmic limb-darkening coefficients ($x_{A,B}$, $y_{A,B}$) were taken from the updated tables of W. Van Hamme (1993) built in the W-D program. The circular orbit ($e = 0$) of the binary target was adopted from the phase differences and the $O - C$ timing residuals of the two minimum types. The binary parameters set free during this modeling are the orbital ephemeris (T_0 , P_{orb}) and inclination (i), semi-major axis (a), center-of-mass velocity (γ), effective temperature of TIC 399725538 B ($T_{B,\text{eff}}$), components' potentials ($\Omega_{A,B}$), luminosity of TIC 399725538 A (l_A), and the third light (l_3).

We performed a q -search over the entire range of known mass ratios for the EL CVn binaries (J. W. Lee et al. 2022a). Specifically, we computed a series of models for fixed q values with a step size of 0.002, which was narrowed to 0.001 in the vicinity of the minimum. At each step, q was held constant while other adjustable parameters were allowed to converge. The mass ratio is primarily constrained by the amplitude of the ellipsoidal modulations in the outside-eclipse light curve, which arises from the tidal distortion of the components (S. L. Morris 1985; S. Bloemen et al. 2012). The weighted sum of squared residuals ($\sum W(O - C)^2$) exhibited a well-defined global minimum near $q = 0.11$. This value was subsequently adopted as the initial input for the final simultaneous solution where q was adjusted as a free parameter. The resulting light and RV parameters are summarized in Table 3. The binary star model indicates that TIC 399725538 is a detached system with fill-out factors of $f_A = 57.1\%$ and $f_B = 41.1\%$, where $f_{A,B} = \Omega_{\text{in}}/\Omega_{A,B}$ and Ω_{in} represents the inner critical Roche potential. Most of the third light $l_3 = 0.136$ comes from two neighboring stars, TIC 399725539 and TIC 399725544, located around our program target, as discussed in the second section. Our synthetic model is presented as red solid curves in the second panel of Figure 1 and the top panel of Figure 3, demonstrating an excellent fit to both the light and RV data.

The simultaneous modeling parameters in Table 3 allow the calculation of the absolute dimensions of TIC 399725538, which are presented in Table 4 with those of Y. Peng et al. (2024). In these computations, we used solar values of $M_{\text{bol}\odot} = +4.73$ and $T_{\text{eff}\odot} = 5780$ K, and obtained the bolometric corrections (BC) using the temperature-dependent calibration of each component (G. Torres 2010). The secondary star parameters of $M_B = 0.211 \pm 0.005 M_\odot$, $R_B = 0.207 \pm 0.005 R_\odot$, $\log g_B = 5.131 \pm 0.020$, and $T_B = 10,935 \pm 110$ K are typical values for pre-ELM WDs in EL CVn systems (P. F. L. Maxted et al. 2014; J. W. Lee et al. 2020). In single-lined EBs, the secondary's surface gravity can be calculated directly from observable quantities (P_{orb} , K_A , e , r_B , i) using the following relation (J. Southworth et al. 2007):

$$g_B = \frac{2\pi}{P_{\text{orb}}} \frac{K_A(1 - e^2)^{1/2}}{r_B^2 \sin i}, \quad (2)$$

where $r_B = R_B/a$ is the fractional radius of the low-mass companion. The surface gravity of $\log g_B = 5.131 \pm 0.026$ calculated from this equation is in perfect agreement with the value (5.131 ± 0.020) derived from our binary modeling through $g_B = GM_B/R_B^2$.

The target distance can be measured using the distance-modulus equation $V - A_V - M_{V,EB} = 5 \log d - 5$. Here, V is the apparent magnitude at maximum light, $A_V \simeq 3.1E(B - V)$ is the interstellar extinction in V band, and $M_{V,EB}$ is the total absolute magnitude of the system, which is the sum of M_{V_A} and M_{V_B} . Using the TESS v8.2 measurements of $V = 11.258 \pm 0.069$ and $E(B - V) = 0.2381 \pm 0.0093$ (M. Paegert et al. 2022), we obtained a geometric distance of 477 ± 19 pc for TIC 399725538. The EB-based distance matches well with the Gaia DR3 distance of 484 ± 6 pc, corresponding to a parallax of $\pi = 2.068 \pm 0.026$ mas (Gaia Collaboration et al. 2023).

5. PULSATION FREQUENCY ANALYSIS

Considering the physical parameters in Table 4, the primary and secondary components of TIC 399725538 can be classified as candidates for intermediate-mass and ELM WD pulsators, respectively (e.g., K. Hong et al. 2021; J. W. Lee et al. 2022a, 2024). However, Y. Peng et al. (2024) reported no detectable pulsation signals in their TESS residual lights. We used the 200-s cadence data from S71 to find possible pulsation frequencies in the binary target. The top panel of Figure 5 shows the time-series light curve residuals from the W-D model fit. We applied the PERIOD04 software package (P. Lenz & M. Breger 2005) to the binary-subtracted residuals, and searched for multiple frequencies up to the Nyquist frequency of 216 day^{-1} through the pre-whitening process (J. W. Lee et al. 2014).

The results of the multi-frequency analysis are summarized in Table 5, and the corresponding amplitude spectra are displayed in the middle and bottom panels of Figure 5. We detected a total of three significant frequencies with $\text{SNR} > 5$ (M. Breger et al. 1993; A. S. Baran & C. Koen 2021), all of which lie within the γ Dor instability region. The model light curve synthesized from these frequencies is indicated by a red solid line in the top panel of this figure. The total timespan of the TESS S71 data used is $\Delta T = 24.2$ days. Using the Rayleigh criterion of $1/\Delta T = 0.041 \text{ day}^{-1}$ as the frequency resolution for identifying aliasing signals, we found that the frequencies f_2 and f_3 correspond to approximately twice and four times f_1 , respectively. After excluding these two harmonics, only the f_1 frequency is identified as a γ Dor-type pulsation intrinsic to TIC 399725538 A.

The TESS S71 residual lights exhibit gaps, including a data-download interruption between BJD 2,460,246.445 and BJD 2,460,248.741. Low-frequency artifacts may arise from uncorrected trends in TESS data or from imperfect removal of binary effects during the W-D modeling. Therefore, it is difficult to completely rule out the possibility that the f_1 frequency is an artifact. Furthermore, the 200-s sampling cadence is insufficient to detect short-period oscillations, such as those characteristic of ELM variables. More accurate short-cadence data will be required to confirm and refine our results through detailed pulsation analysis.

6. DISCUSSION AND CONCLUSIONS

For the TESS target TIC 399725538, classified as an EL CVn EB, we conducted time-series spectroscopy using the echelle spectrographs mounted on 2-m class telescopes in Korea and Thailand, respectively, securing a total of 33 spectra. We constructed BF profiles from the target spectra, showing only the peak corresponding to the primary component A. Despite the relatively low SNRs

of the spectra, the absence of any detectable signal from the secondary companion indicates its extremely low light contribution (l_B) and mass ratio (q). The RVs of TIC 399725538 A were derived by fitting the BF profiles with a rotational broadening function, and its atmospheric parameters were found to be $T_{\text{eff},A} = 7194 \pm 70$ K and $v_A \sin i = 68 \pm 9$ km s $^{-1}$ by applying the **GSSP** package to a representative spectrum reconstructed using **shift-and-add disentangling** code. The ground-based spectroscopic measurements were combined with the time-series photometric data from TESS S32 and S71, yielding the following parameters for each component: $M_A = 1.930 \pm 0.054 M_\odot$, $R_A = 1.922 \pm 0.020 R_\odot$, $T_{\text{eff},A} = 7194 \pm 70$ K, and $L_A = 8.87 \pm 0.39 L_\odot$ for TIC 399725538 A; and $M_B = 0.211 \pm 0.005 M_\odot$, $R_B = 0.207 \pm 0.005 R_\odot$, $T_{\text{eff},B} = 10,935 \pm 110$ K, and $L_B = 0.546 \pm 0.034 L_\odot$ for TIC 399725538 B.

The absolute parameters indicate that TIC 399725538 is a typical EL CVn star, characterized by a short P_{orb} and low (q , M_B) combination (P. F. L. Maxted et al. 2014; J. van Roestel et al. 2018; J. W. Lee et al. 2020; Ö. Çakirli et al. 2024). If ELM WDs evolve through stable Roche-lobe overflow and their progenitors possess degenerate cores, a tight correlation would be expected between the He-core WD masses (M_{WD}) and the orbital periods (P_{orb}) (J. Lin et al. 2011; X. Chen et al. 2017). The position of TIC 399725538 B on the $\log P_{\text{orb}} - M_{\text{WD}}$ plot is shown in Figure 6, along with the low-mass companions of short-period (< 10 days) double-lined EL CVn and R CMa EBs (J. W. Lee & J.-H. Park 2018; J. W. Lee et al. 2018, 2020, 2022b, 2024, 2025; K. Wang et al. 2019; L. Wang et al. 2020; S.-L. Kim et al. 2021; K. Hong et al. 2021; Ö. Çakirli et al. 2024; M. Kovalev et al. 2024). In this figure, the pre-ELM WDs closely follow the $\log P_{\text{orb}} - M_{\text{WD}}$ relationship from J. Lin et al. (2011), supporting the prediction that the He-core WDs are formed in binary systems through non-conservative mass transfer (X. Chen et al. 2017).

Comparing the binary parameters to stellar models provides a straightforward means of assessing whether observations are consistent with theoretical predictions. To examine the current evolutionary state of our program target, we employed the Hertzsprung-Russell (H-R) diagram presented in Figure 7, where the cyan and pink crosses denote the primary (A) and secondary (B) components, respectively. TIC 399725538 A is located within the overlapping instability region of the main-sequence δ Sct and γ Dor variables, suggesting that it is a candidate intermediate-mass pulsator. In the same figure, the solid black curves represent the evolutionary sequences for WD masses of $0.1611 M_\odot$, $0.1706 M_\odot$, $0.1821 M_\odot$, $0.1921 M_\odot$, and $0.2025 M_\odot$ from L. G. Althaus et al. (2013). The pre-ELM WD companion of TIC 399725538 corresponds to an evolutionary track of $0.1706 M_\odot$, which is about 19 % less massive than our measured value. A similar trend is observed when employing the ELM WD models of A. G. Istrate et al. (2016), which account for both element diffusion and rotation mixing. These results indicate that TIC 399725538 B is significantly underluminous relative to its mass in the context of He-core WD evolution. The origin of the discrepancy between the target measurements and the ELM WD models remains unclear. However, it may stem from the lack of certain detailed physical processes in the WD formation models, or from unresolved binary evolution effects, such as non-conservative mass transfer.

The population membership of WDs can be obtained through the classification scheme of E.-M. Pauli et al. (2006), which is based on the $U - V$ and $J_z - e$ diagrams. Following the procedure applied in J. W. Lee et al. (2020, 2024), we calculated the space velocities and Galactic orbital

parameters of TIC 399725538 as $(U, V, W)^6 = (-86.6 \pm 0.2, +175.0 \pm 0.5, -33.0 \pm 0.1)$ km s⁻¹ and $(J_z, e)^7 = (1484 \pm 18 \text{ kpc km s}^{-1}, 0.3282 \pm 0.0004)$. These calculations used our systemic velocity γ in conjunction with the Gaia measurements (Gaia Collaboration et al. 2023). The location of TIC 399725538 in both diagrams suggests that the EL CVn EB is a member of the thick-disk population. This represents the third such system identified among well-studied EL CVn stars to date, following WASP 0247-25 (P. F. L. Maxted et al. 2014) and WASP 0346-21 (J. W. Lee et al. 2024).

Through the non-conservative mass transfer (X. Chen et al. 2017), the initially more massive component of TIC 399725538 evolved into the present He-core WD precursor, while the mass gainer transformed into a potentially intermediate-mass, pulsating main-sequence star via accretion. TIC 399725538 B is currently in the pre-ELM WD stage, evolving toward higher T_{eff} at nearly constant L before reaching a fully formed WD phase and subsequently entering the cooling sequence. Using the $M_{\text{WD}} - t$ relation from X. Chen et al. (2017), we estimate its lifetime during this stage to be approximately 1.2×10^8 yr. Given that EL CVn-type binaries with reliable physical parameters remain rare, follow-up spectroscopic observations of poorly characterized targets are essential for elucidating the formation and evolution of these intriguing systems. In particular, high-resolution echelle spectroscopy using medium-to-large aperture telescopes, such as the VLT/UVES (e.g. Ö. Çakirli et al. 2024; J. W. Lee et al. 2024, 2025), will be crucial for detecting the low-mass companions and constraining their properties, especially considering the short orbital periods and high luminosity contrast that characterize EL CVn systems.

¹ This study utilizes echelle spectra obtained at the BOAO in Korea and the TNO in Thailand, together with light curves from the TESS mission. The TNO spectra were acquired with the MRRES spectrograph under program ID TNTC12_022. The authors thank the anonymous referee for providing insightful and constructive comments, which significantly improved the clarity and depth of the manuscript. We gratefully acknowledge support from the KASI grant 2026-1-904-01.

⁶ Positive toward the Galactic center, Galactic rotation, and North Galactic Pole.

⁷ Angular momentum in the z direction and eccentricity

REFERENCES

Althaus, L. G., Miller Bertolami, M. M., & C  sico, A. H. 2013, A&A, 557, A19, doi: [10.1051/0004-6361/201321868](https://doi.org/10.1051/0004-6361/201321868)

Baran, A. S., & Koen, C. 2021, AcA, 71, 113, doi: [10.32023/0001-5237/71.2.3](https://doi.org/10.32023/0001-5237/71.2.3)

Blanco-Cuaresma, S., Soubiran, C., Heiter, U., et al. 2014, A&A, 569, A111, doi: [10.1051/0004-6361/201423945](https://doi.org/10.1051/0004-6361/201423945)

Bloemen, S., Marsh, T. R., Degroote, P., et al. 2012, MNRAS, 422, 2600, doi: [10.1111/j.1365-2966.2012.20818.x](https://doi.org/10.1111/j.1365-2966.2012.20818.x)

Breger, M., Stich, J., Garrido, R., et al. 1993, A&A, 271, 482, doi: [10.1051/0004-6361:1993271482](https://doi.org/10.1051/0004-6361:1993271482)

Buisset, C., Poshyachinda, S., Soonthornthum, B., et al. 2018, Proc. SPIE, doi: [10.1117/12.2299493](https://doi.org/10.1117/12.2299493)

  akirli,   ., Hoymen, B., &   zdarcan, O. 2024, MNRAS, 533, 2058 doi: [10.1093/mnras/stae1948](https://doi.org/10.1093/mnras/stae1948)

Chen, X., Maxted, P. F. L., Li, J., & Han, Z. 2017, MNRAS, 467, 1874, doi: [10.1093/mnras/stx115](https://doi.org/10.1093/mnras/stx115)

Coelho, P., Barbuy, B., Melendez, J., Sciauon, R. P., & Castilho, B. V. 2005, A&A, 443, 735, doi: [10.1051/0004-6361:20053511](https://doi.org/10.1051/0004-6361:20053511)

Errmann, R., Cook, N., Anglada-Escud  , G., et al. 2020, PASP, 132, 064504, doi: [10.1088/1538-3873/ab8783](https://doi.org/10.1088/1538-3873/ab8783)

Gaia Collaboration, Vallenari A., Brown A. G. A., et al. 2023, A&A, 674, A1, doi: [10.1051/0004-6361/202243940](https://doi.org/10.1051/0004-6361/202243940)

Hong, K., Lee, J. W., Koo, J.-R., et al. 2021, AJ, 161, 137, doi: [10.3847/1538-3881/abdd39](https://doi.org/10.3847/1538-3881/abdd39)

Istrate, A. G., Marchant, P., Tauris, T. M., et al. 2016, A&A, 595, A35, doi: [10.1051/0004-6361/201628874](https://doi.org/10.1051/0004-6361/201628874)

Jenkins, J. M., Twicken, J. D., McCauliff, S., et al. 2016, Proc. SPIE, 9913, 99133E, doi: [10.1117/12.2233418](https://doi.org/10.1117/12.2233418)

Kallinger, T., Reegen, P., & Weiss, W. W. 2008, A&A, 481, 571, doi: [10.1051/0004-6361:20077559](https://doi.org/10.1051/0004-6361:20077559)

Kallrath, J. 2022, Galaxies, 10, 17, doi: [10.3390/galaxies10010017](https://doi.org/10.3390/galaxies10010017)

Kilic, M., Stanek, K. Z., & Pinsonneault, M. H. 2007, ApJ, 671, 761, doi: [10.1086/522228](https://doi.org/10.1086/522228)

Kim, K.-M., Han, I., Valyavin, G. G., et al. 2007, PASP, 119, 1052, doi: [10.1086/521959](https://doi.org/10.1086/521959)

Kim, S.-L., Lee, J. W., Lee, C.-U., et al. 2021, AJ, 162, 212, doi: [10.3847/1538-3881/ac23de](https://doi.org/10.3847/1538-3881/ac23de)

Kovalev, M., Li, Z., Xiong, J., et al. 2024, MNRAS, 535, 2651, doi: [10.1093/mnras/stae2494](https://doi.org/10.1093/mnras/stae2494)

Kwee, K. K., & Van Woerden, H. 1956, Bull. Astron. Inst. Netherlands, 12, 327

Lagos, F., Schreiber, M. R., Parsons, S. G., et al. 2020, MNRAS, 499, L121, doi: [10.1093/mnrasl/slaa164](https://doi.org/10.1093/mnrasl/slaa164)

Lee, J. W., & Park, J.-H. 2018, MNRAS, 480, 4693, doi: [10.1093/mnras/sty2153](https://doi.org/10.1093/mnras/sty2153)

Lee, J. W., Hong, K., Jeong, M.-J., & Wolf, M. 2024, ApJ, 973, 113, doi: [10.3847/1538-4357/ad67c7](https://doi.org/10.3847/1538-4357/ad67c7)

Lee, J. W., Hong, K., Kim, H.-Y., & Park, J.-H. 2022a, MNRAS, 515, 4702, doi: [10.1093/mnras/stac2151](https://doi.org/10.1093/mnras/stac2151)

Lee, J. W., Hong, K., Koo, J.-R., & Park J.-H., 2018, AJ, 155, 5, doi: [10.3847/1538-3881/aa947e](https://doi.org/10.3847/1538-3881/aa947e)

Lee, J. W., Hong, K., & Park, J.-H. 2022b, MNRAS, 511, 654, doi: [10.1093/mnras/stac075](https://doi.org/10.1093/mnras/stac075)

Lee, J. W., Jeong, M.-J., & Hong, K. 2025, MNRAS, 538, 3314, doi: [10.1093/mnras/staf473](https://doi.org/10.1093/mnras/staf473)

Lee, J. W., Kim, S.-L., Hong, K., Lee, C.-U., & Koo, J.-R. 2014, AJ, 148, 37, doi: [10.1088/0004-6256/148/2/37](https://doi.org/10.1088/0004-6256/148/2/37)

Lee, J. W., Koo, J.-R., Hong, K., & Park, J.-H. 2020, AJ, 160, 49, doi: [10.3847/1538-3881/ab9621](https://doi.org/10.3847/1538-3881/ab9621)

Lee, J. W., Kristiansen, M., & Hong, K. 2019, AJ, 157, 223, doi: [10.3847/1538-3881/ab1a3b](https://doi.org/10.3847/1538-3881/ab1a3b)

Lee, J. W., Youn, J.-H., Kim, C.-H., Lee, C.-U., & Kim, H.-I. 2008, AJ, 135, 1523, doi: [10.1088/0004-6256/135/4/1523](https://doi.org/10.1088/0004-6256/135/4/1523)

Lehmann, H., Tkachenko, A., Semaan, T., et al. 2011, A&A, 526, A124, doi: [10.1051/0004-6361/201015769](https://doi.org/10.1051/0004-6361/201015769)

Lenz, P., & Breger, M. 2005, Comm. Asteroseismology, 146, 53, doi: [10.1553/cia146s53](https://doi.org/10.1553/cia146s53)

Lin, J., Rappaport, S., Podsiadlowski, P., et al. 2011, ApJ, 732, 70, doi: [10.1088/0004-637X/732/2/70](https://doi.org/10.1088/0004-637X/732/2/70)

Marsh, T. R., Dhillon, V. S., & Duck, S. R. 1995, MNRAS, 275, 828, doi: [10.1093/mnras/275.3.828](https://doi.org/10.1093/mnras/275.3.828)

Maxted, P. F. L., Bloemen, S., Heber, U., et al. 2014, MNRAS, 437, 1681, doi: [10.1093/mnras/stt2007](https://doi.org/10.1093/mnras/stt2007)

Maxted, P. F. L., Serenelli, A. M., Miglio, A., et al. 2013, Natur, 498, 463, doi: [10.1038/nature12192](https://doi.org/10.1038/nature12192)

Morris, S. L. 1985, ApJ, 295, 143, doi: [10.1086/163359](https://doi.org/10.1086/163359)

Mowlavi, N., Holl, B., Lecoeur-Taïbi, I., et al. 2023, A&A, 674, A16, doi: [10.1051/0004-6361/202245330](https://doi.org/10.1051/0004-6361/202245330)

Paegert, M., Stassun, K. G., Collins, K. A., et al. 2022, VizieR Online Data Catalog, IV/39

Pauli, E.-M., Napiwotzki, R., Heber, U., Altmann, M., & Odenkirchen, M. 2006, A&A, 447, 173, doi: [10.1051/0004-6361:20052730](https://doi.org/10.1051/0004-6361:20052730)

Peng, Y., Wang, K., Ren, A., 2024, NewA, 107, 102153, doi: [10.1016/j.newast.2023.102153](https://doi.org/10.1016/j.newast.2023.102153)

Pilecki, B., Konorski, P., & Gorski, M. 2012, in IAU Symp. 282, From Interacting Binaries to Exoplanets: Essential Modeling Tools, ed. M. T. Richards, & I. Hubeny (Cambridge: Cambridge Univ. Press), 301, doi: [10.1017/S174392131102761X](https://doi.org/10.1017/S174392131102761X)

Ricker, G. R., Winn, J. N., Vanderspek, R., et al. 2015, JATIS, 1, 014003, doi: [10.1111/jat.1.014003](https://doi.org/10.1111/jat.1.014003)

Rittipruk, P., Hong, K., Lee, J. W., et al. 2025, AJ, 169, 66, doi: [10.3847/1538-3881/ad99ce](https://doi.org/10.3847/1538-3881/ad99ce)

Różański, T., Niemczura, E., Lemiesz, J., et al. 2022, A&A, 659, A199, doi: [10.1051/0004-6361/202141480](https://doi.org/10.1051/0004-6361/202141480)

Rucinski, S. M. 1969, Acta. Astron., 19, 125

Rucinski, S. M. 1992, AJ, 104, 1968, doi: [10.1051/0004-6361/201015769](https://doi.org/10.1051/0004-6361/201015769)

Rucinski, S. M. 2002, AJ, 124, 1746, doi: [10.1086/342342](https://doi.org/10.1086/342342)

Shenar, T., Bodensteiner, J., Abdul-Masih, M., et al. 2020, A&A, 639, L6, doi: [10.1051/0004-6361/202038275](https://doi.org/10.1051/0004-6361/202038275)

Shenar, T., Sana, H., Mahy, L., et al. 2022, A&A, 665, A148, doi: [10.1051/0004-6361/202244245](https://doi.org/10.1051/0004-6361/202244245)

Shulyak, D., Tsymbal, V., Ryabchikova, T., et al. 2004, A&A, 428, 993, doi: [10.1051/0004-6361:20034169](https://doi.org/10.1051/0004-6361:20034169)

Southworth, J., Wheatley, P. J., Sams, G. 2007, MNRAS, 379, L11, doi: [10.1111/j.1745-3933.2007.00324.x](https://doi.org/10.1111/j.1745-3933.2007.00324.x)

Tkachenko, A. 2015, A&A, 581, A129, doi: [10.1051/0004-6361/201526513](https://doi.org/10.1051/0004-6361/201526513)

Torres, G. 2010, AJ, 140, 1158, doi: [10.1088/0004-6256/140/5/1158](https://doi.org/10.1088/0004-6256/140/5/1158)

Tsymbal, V. 1996, in ASP Conf. Ser. 108, M.A.S.S., Model Atmospheres and Spectrum Synthesis, ed. S. J. Adelman, F. Kupka, & W. W. Weiss (San Francisco, CA: ASP), 198

Van Hamme, W. 1993, AJ, 106, 209, doi: [10.1086/116788](https://doi.org/10.1086/116788)

van Roestel, J., Kupfer, T., Ruiz-Carmona, R., et al. 2018, MNRAS, 475, 2560, doi: [10.1093/mnras/stx3291](https://doi.org/10.1093/mnras/stx3291)

Von Zeipel, H., 1924, MNRAS, 84, 665, doi: [10.1093/mnras/84.9.665](https://doi.org/10.1093/mnras/84.9.665)

Wang, K., Zhang, X., Luo, Y., Luo, C. 2019, MNRAS, 486, 2462, doi: [10.1093/mnras/stz1033](https://doi.org/10.1093/mnras/stz1033)

Wang, L., Gies, D. R., Lester, K. V., et al. 2020, AJ, 159, 4, doi: [10.3847/1538-3881/ab52fa](https://doi.org/10.3847/1538-3881/ab52fa)

Wilson, R. E., & Devinney, E. J. 1971, ApJ, 166, 605, doi: [10.1086/150986](https://doi.org/10.1086/150986)

Xiong, J., Li, Z., Li, J., et al. 2025, ApJ, 979, 108, doi: [10.3847/1538-4357/ad9b9c](https://doi.org/10.3847/1538-4357/ad9b9c)

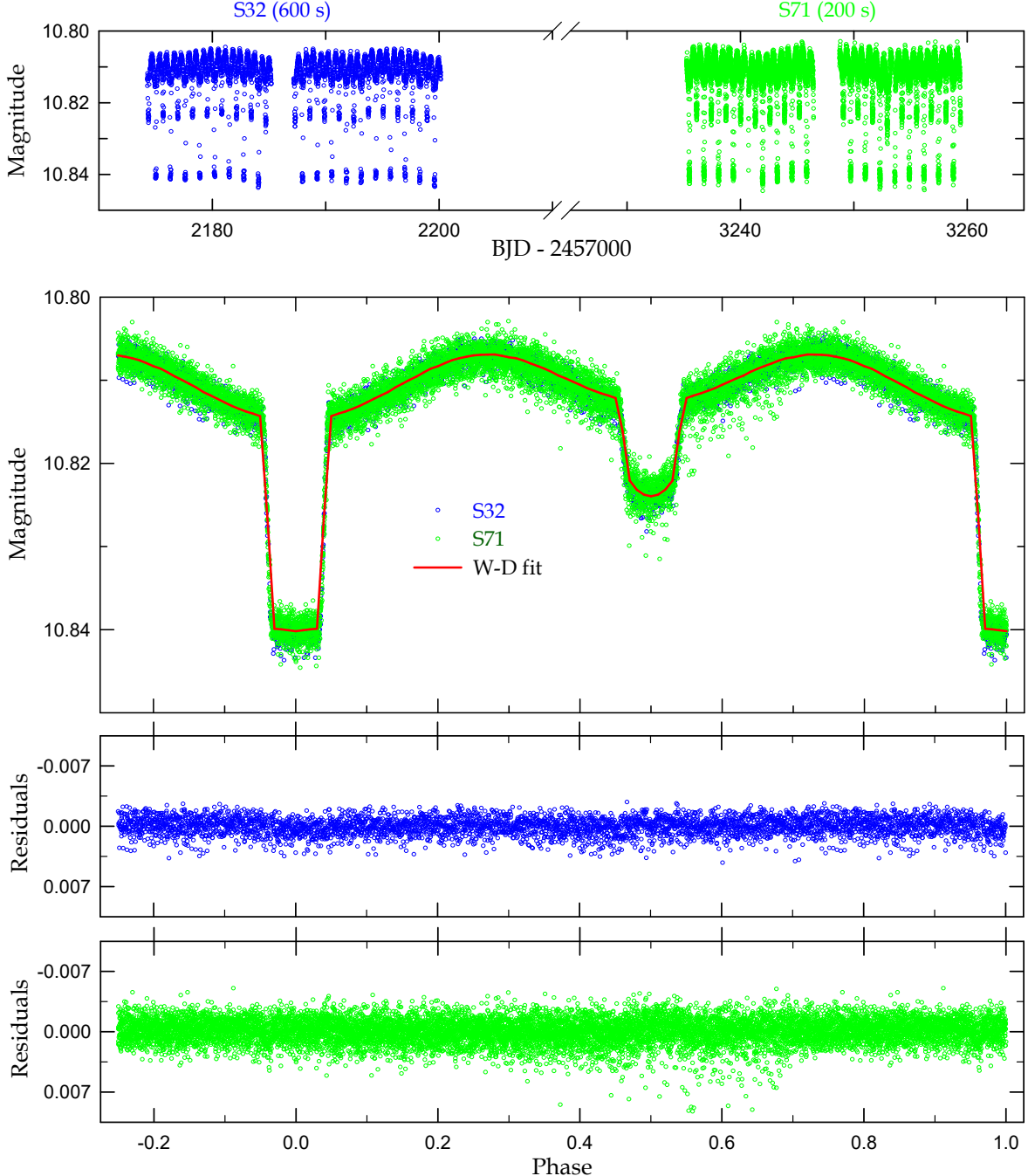


Figure 1. TESS observations of TIC 399725538 distributed in BJD (top panel) and orbital phase (second panel). The blue and green circles are individual measurements for Sectors 32 and 71, respectively, and the red solid curve represents the synthetic model obtained through our W-D fit. The third and bottom panels show the residual lights corresponding to the binary model curve.

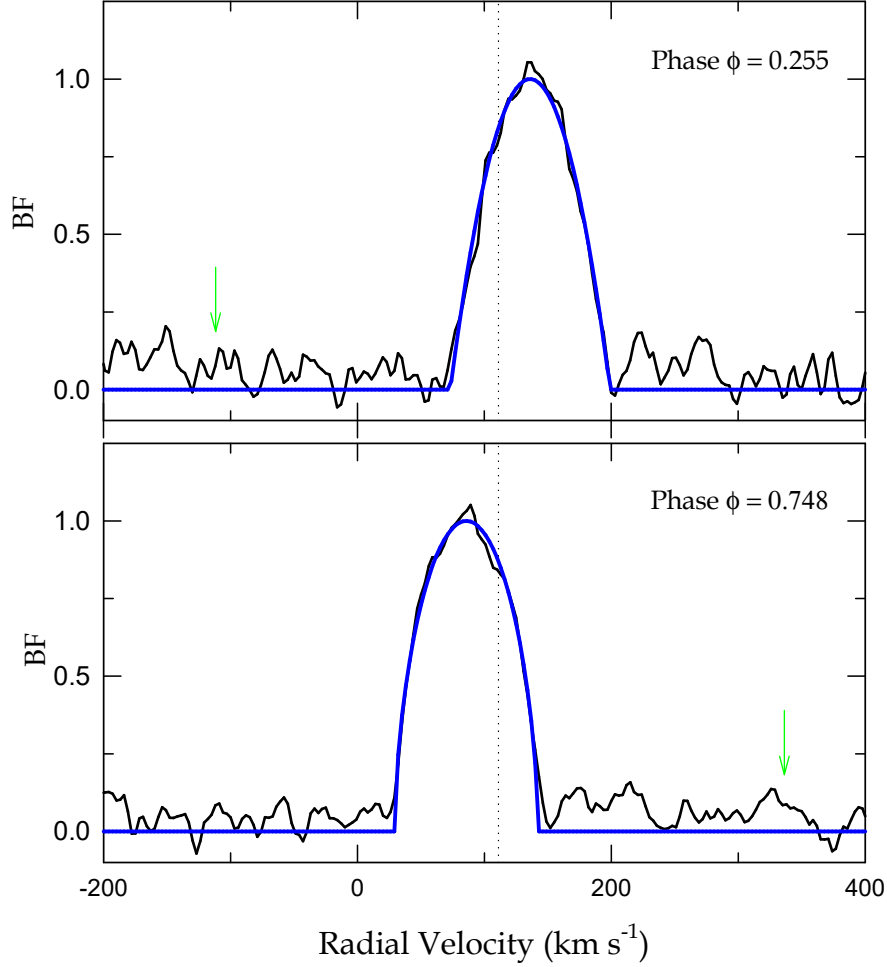


Figure 2. Sample of the BF profiles. The black lines are the observed BFs for two orbital phases (ϕ), with a single peak representing the primary component. A rotational broadening function applied to this peak is plotted as the solid blue line. The vertical dotted lines represent the radial velocity of the binary center of mass, and the green arrows point to the RV positions of the secondary companion predicted by our binary modeling.

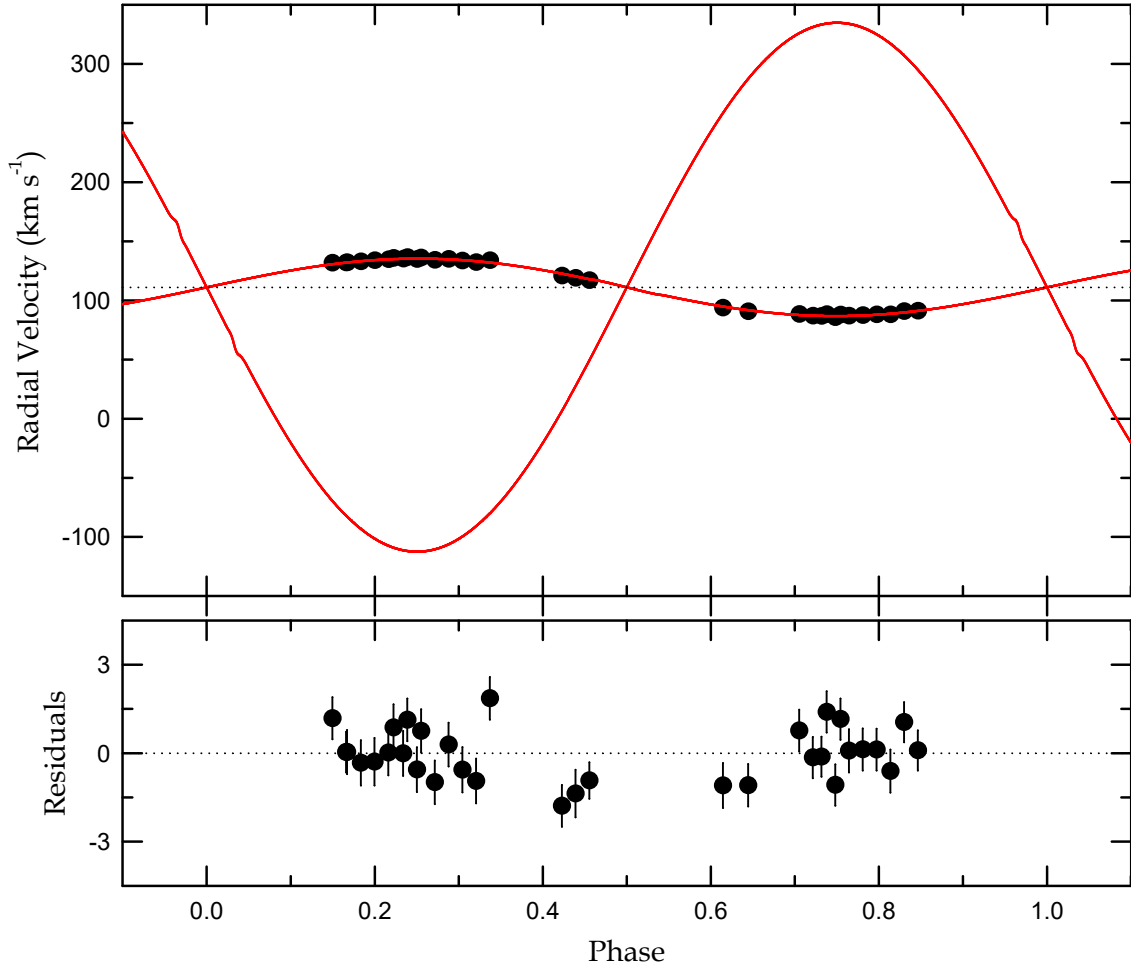


Figure 3. Radial velocities of TIC 399725538 A. The solid curves represent the results from a consistent light and RV curve analysis, and the dotted line denotes the systemic velocity of $+111.12 \text{ km s}^{-1}$. The lower panel displays the residuals between observations and models.

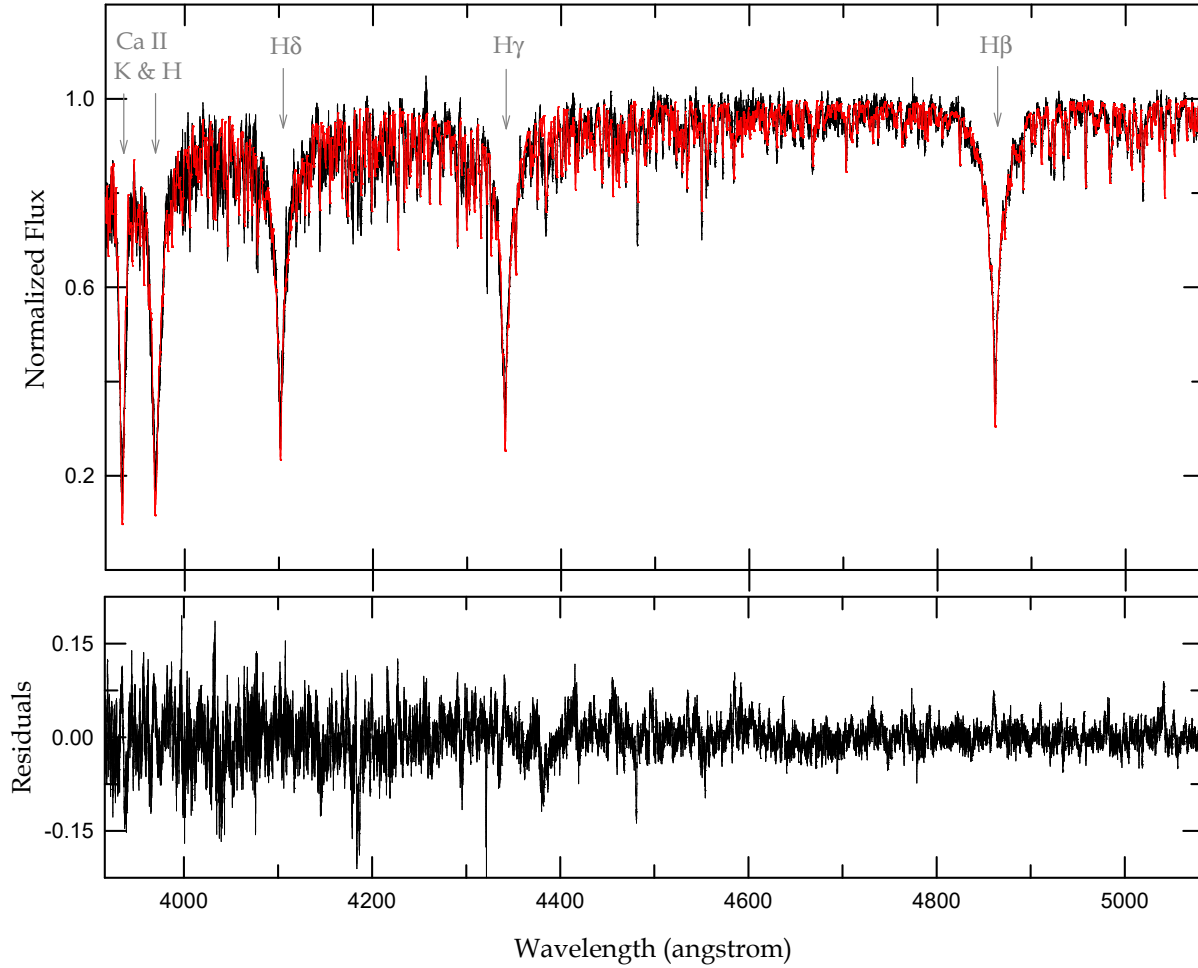


Figure 4. Reconstructed spectrum of TIC 399725538 A. The black and red solid lines represent the disentangled and best-fitting synthetic spectra, respectively. The lower panel displays the residuals between the two.

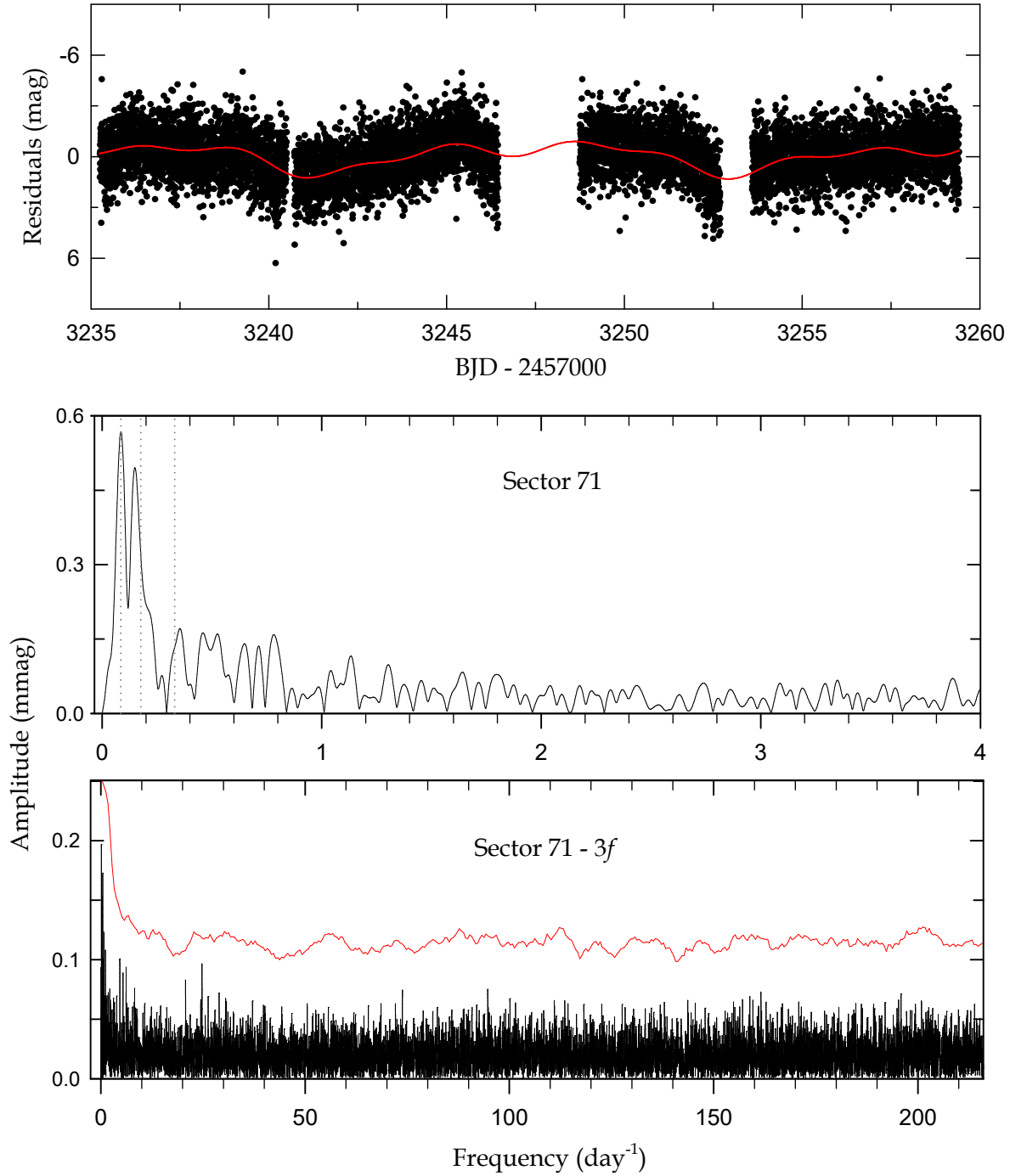


Figure 5. The top panel shows the light curve residuals of TESS S71 distributed in BJD. The middle and bottom panels are amplitude spectra before and after prewhitening all three frequencies extracted from the full residuals using the `PERIOD04` code. The synthetic model curve for these frequencies is indicated by the red solid line in the top panel. The vertical dotted lines in the middle panel indicate the positions of the extracted frequencies and the red line in the bottom panel represents five times the noise spectrum.

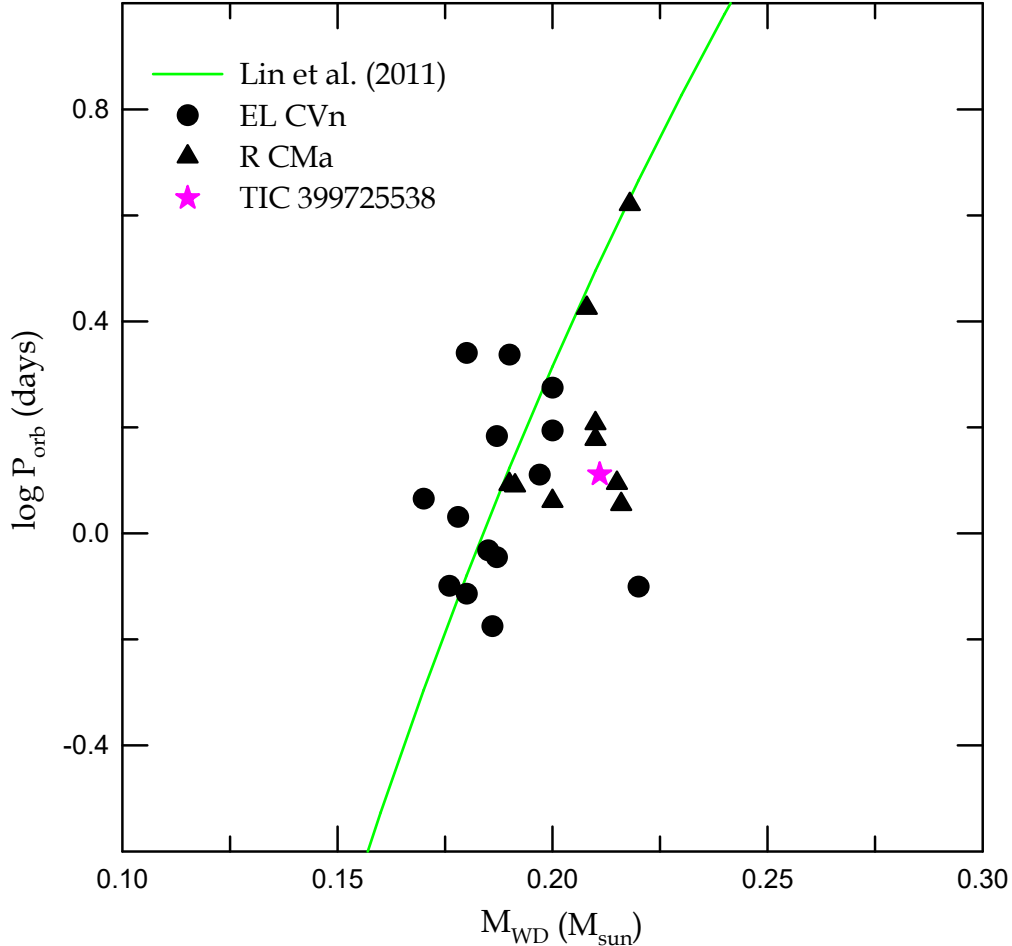


Figure 6. $\log P_{\text{orb}} - M_{\text{WD}}$ diagram for TIC 399725538 B (star symbol) and the other pre-ELM WD companions in double-lined EL CVn-type (circles) and R CMa-type (triangles) binaries, respectively. The green solid line represents the relationship for the stable mass transfer evolution presented by [J. Lin et al. \(2011\)](#).

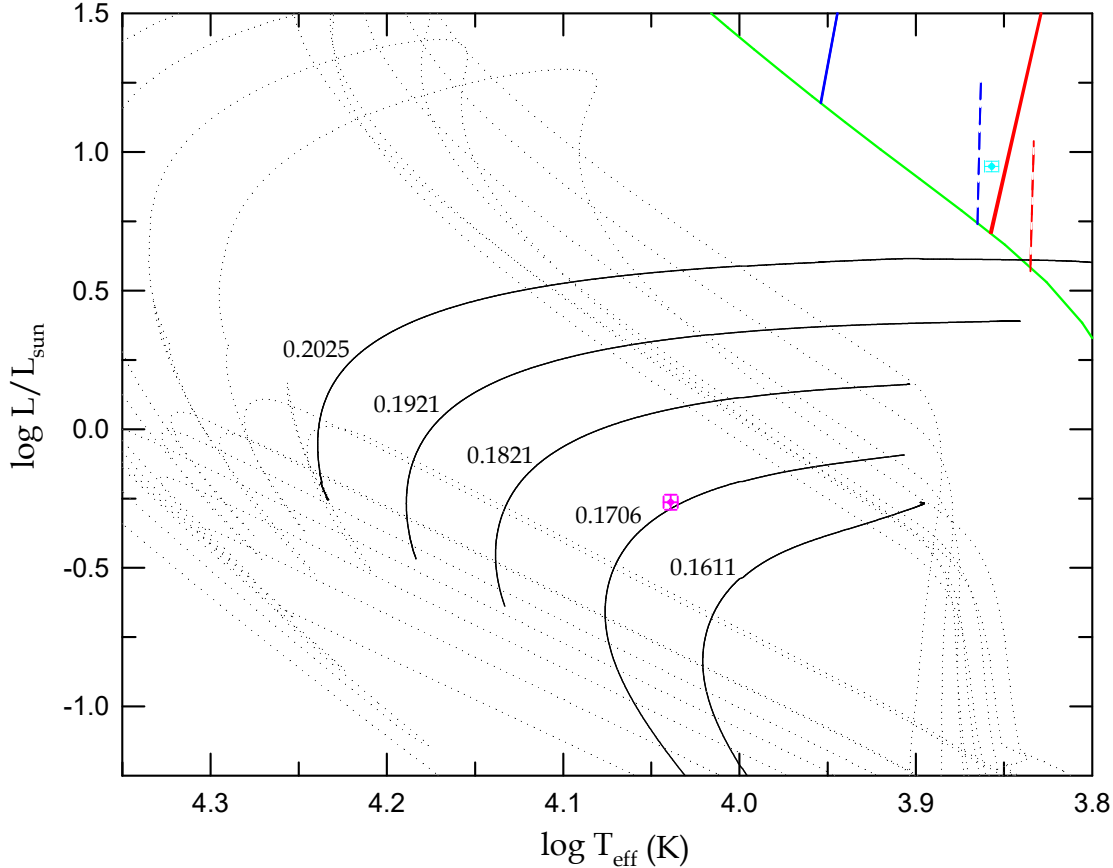


Figure 7. Position of TIC 399725538 A (cyan cross) and B (pink cross) in the H-R diagram. The green solid line represents the zero-age main sequence, while the colored oblique solid and dashed lines indicate the instability strips of δ Sct and γ Dor stars, respectively (see [J. W. Lee et al. 2024](#)). The black solid lines denote the evolutionary sequences of ELM WDs with masses from $0.1611 M_{\odot}$ to $0.2025 M_{\odot}$, up to the first occurrence points of CNO flashes ([L. G. Althaus et al. 2013](#)). The dotted gray line shows the full evolutionary track of the $0.2025 M_{\odot}$ model.

Table 1. TESS Eclipse Timings of TIC 399725538

BJD	Error	Epoch	$O - C$	Min
2,459,174.35735	± 0.00073	-820.5	-0.00144	II
2,459,175.00550	± 0.00026	-820.0	+0.00007	I
2,459,175.65159	± 0.00052	-819.5	-0.00048	II
2,459,176.29824	± 0.00038	-819.0	-0.00047	I
2,459,176.94625	± 0.00048	-818.5	+0.00091	II
2,459,177.59241	± 0.00021	-818.0	+0.00043	I
2,459,178.23721	± 0.00071	-817.5	-0.00141	II
2,459,178.88574	± 0.00026	-817.0	+0.00048	I
2,459,179.53301	± 0.00177	-816.5	+0.00111	II
2,459,180.17805	± 0.00027	-816.0	-0.00049	I

NOTE—This table is available in its entirety in machine-readable form. A portion is shown here for guidance regarding its form and content.

Table 2. Radial Velocities of TIC 399725538 A

BJD (2,460,000+)	V_A (km s $^{-1}$)	σ_A (km s $^{-1}$)	Spectrograph
259.0603	+135.87	0.79	BOES
259.0815	+136.46	0.72	BOES
259.1027	+136.16	0.73	BOES
259.1238	+134.24	0.74	BOES
259.1450	+135.09	0.74	BOES
259.1662	+133.56	0.77	BOES
259.1874	+132.26	0.76	BOES
259.2086	+133.91	0.72	BOES
259.3195	+120.88	0.71	BOES
259.3407	+119.00	0.81	BOES
259.3619	+117.07	0.62	BOES
264.1393	+131.84	0.71	BOES
264.1605	+132.06	0.69	BOES
317.9167	+86.84	0.68	BOES
317.9378	+85.75	0.70	BOES
317.9590	+87.03	0.73	BOES
317.9803	+87.45	0.71	BOES
318.0015	+88.07	0.71	BOES
318.0226	+88.20	0.73	BOES
318.0438	+90.95	0.68	BOES
318.0650	+91.31	0.68	BOES
322.9381	+93.81	0.76	BOES
322.9770	+90.69	0.72	BOES
379.9596	+88.47	0.71	BOES
379.9808	+87.02	0.70	BOES
380.0020	+88.28	0.70	BOES
380.0232	+88.00	0.70	BOES
683.1844	+132.15	0.75	MRES
683.2055	+132.92	0.77	MRES
683.2267	+133.86	0.81	MRES
683.2478	+134.83	0.77	MRES
683.2707	+135.25	0.76	MRES
683.2918	+134.85	0.76	MRES

Table 3. Light and Velocity Parameters of TIC 399725538

Parameter	Primary (A)	Secondary (B)
T_0 (HJD)	2,460,235.49365 \pm 0.00034	
P_{orb} (day)	1.29327822 \pm 0.00000082	
a (R_{\odot})		6.436 \pm 0.058
γ (km s $^{-1}$)		111.12 \pm 0.24
K_A (km s $^{-1}$)		24.41 \pm 0.37
K_B (km s $^{-1}$)		223.7 \pm 2.2
q		0.1091 \pm 0.0020
i (deg)		80.09 \pm 0.16
T_{eff} (K)	7194 \pm 70	10,935 \pm 110
Ω	3.485 \pm 0.018	4.840 \pm 0.027
Ω_{in}		1.986
F	0.92 \pm 0.12	1.0
x, y	0.518, 0.284	0.390, 0.192
$l/(l_A + l_B + l_3)$	0.8415 \pm 0.0040	0.0225
l_3^b		0.1359 \pm 0.0033
r (pole)	0.2954 \pm 0.0016	0.0320 \pm 0.0007
r (point)	0.3016 \pm 0.0018	0.0321 \pm 0.0007
r (side)	0.2998 \pm 0.0017	0.0321 \pm 0.0007
r (back)	0.3009 \pm 0.0018	0.0321 \pm 0.0007
r (volume) ^c	0.2988 \pm 0.0017	0.0321 \pm 0.0007

^aValue at 0.25 orbital phase.

^bMean volume radius.

Table 4. Absolute Parameters of TIC 399725538

Parameter	Y. Peng et al. (2024)		This Work	
	Primary	Secondary	Primary	Secondary
$M (M_{\odot})$	1.77 ± 0.23	0.139 ± 0.019	1.930 ± 0.054	0.211 ± 0.005
$R (R_{\odot})$	2.14 ± 0.11	0.237 ± 0.013	1.922 ± 0.020	0.207 ± 0.005
$\log g$ (cgs)	4.024 ± 0.029	4.827 ± 0.056	4.156 ± 0.010	5.131 ± 0.020
$\rho (\rho_{\odot})$			0.273 ± 0.010	24.0 ± 1.8
v_{sync} (km s $^{-1}$)			75.18 ± 0.80	8.08 ± 0.19
$vsini$ (km s $^{-1}$)				68 ± 9
T_{eff} (K)	7398 ± 83	$10,740 \pm 120$	7194 ± 70	$10,935 \pm 110$
$L (L_{\odot})$	12.3 ± 1.8	0.67 ± 0.10	8.87 ± 0.39	0.546 ± 0.034
M_{bol} (mag)			2.362 ± 0.048	5.387 ± 0.067
BC (mag)			0.034 ± 0.001	-0.452 ± 0.024
M_V (mag)			2.328 ± 0.048	5.839 ± 0.072
Distance (pc)				477 ± 19

Table 5. Multi-frequency Analysis for TIC 399725538^a

	Frequency (day $^{-1}$)	Amplitude (mmag)	Phase (rad)	SNR ^b	Remark
f_1	0.0848 ± 0.0010	0.695 ± 0.087	5.47 ± 0.37	13.73	
f_2	0.1758 ± 0.0017	0.427 ± 0.086	2.49 ± 0.59	8.50	$2f_1$
f_3	0.3310 ± 0.0026	0.269 ± 0.085	3.07 ± 0.93	5.39	$4f_1$

^aParameter errors were calculated following T. Kallinger et al. (2008).

^bCalculated in a range of 5 day $^{-1}$ around each frequency.